

1 Postprint of: Saidi T., Palmowski D., Babicz-Kiewlicz S., Welearegay T. G., El Bari N.,
2 Ionescu R., Smulko J., Bouchikhi B., Exhaled breath gas sensing using pristine and
3 functionalized WO₃ nanowire sensors enhanced by UV-light irradiation, Sensors and
4 Actuators B: Chemical, Vol. 273 (2018), pp. 1719-1729, DOI: [10.1016/j.snb.2018.07.098](https://doi.org/10.1016/j.snb.2018.07.098)
5 © 2018. This manuscript version is made available under the CC-BY-NC-ND 4.0 license
6 <http://creativecommons.org/licenses/by-nc-nd/4.0/>

8 **Exhaled breath gas sensing using pristine and functionalised** 9 **WO₃ nanowire sensors enhanced by UV-light irradiation**

10 Tarik Saidi^{a, b}, Dariusz Palmowski^c, Sylwia Babicz-Kiewlicz^c, Nezha El Bari^b, Tesfalem
11 Geremariam Welearegay^d, Radu Ionescu^e, Janusz Smulko^c, Benachir Bouchikhi^{a, *}

12 ^a*Sensor Electronic & Instrumentation Group, Moulay Ismail University, Faculty of Sciences,*
13 *Department of Physics, B.P. 11201, Zitoune, Meknes, Morocco*

14 ^b*Biotechnology Agroalimentary and Biomedical Analysis Group, Moulay Ismail University, Faculty of*
15 *Sciences, Department of Biology, B.P. 11201, Zitoune, Meknes, Morocco*

16 ^c*Department of Metrology and Optoelectronics, Gdańsk University of Technology, Gdańsk, Poland*

17 ^d*Department of Electronics, Electrical and Automatic Engineering, Rovira i Virgili University,*
18 *Tarragona 43007, Spain*

19 ^e*The Ångström Laboratory, Department of Solid State Physics, Uppsala University, 75121 Uppsala,*
20 *Sweden*

*Corresponding author:

Postal address: B.P. 11201, Zitoune 50003 Meknes

Tel: +212 535 53 88 70; Fax: +212 535 53 68 08

benachir.bouchikhi@gmail.com

22 **Abstract**

23 The development of advanced metal-oxide-semiconductor (MOS) sensing technologies for the
24 detection of volatile organic compounds (VOCs) present in the exhaled breath is of great
25 importance for non-invasive, cheap and fast medical diagnostics. Our experimental studies
26 investigate the effects of operating temperature selection and UV-light irradiation on improving
27 the sensitivity of WO₃ nanowire sensors for exhaled breath exposure. Herein, six WO₃ nanowire
28 sensors (both pristine and doped with a range of metal nanoparticles such as Pt, Au, Au/Pt, Ni
29 and Fe) were synthesised via aerosol-assisted chemical vapour deposition (AACVD) and
30 characterised by means of atomic force microscopy (AFM), scanning electron microscopy
31 (SEM), transmission electron microscopy (TEM) and energy dispersive X-ray (EDX-ray).
32 Breath measurements were performed in the dark and under UV-light irradiation at various
33 sensor operating temperatures. The results demonstrate that UV-light irradiation combined with
34 the optimisation of the sensors' operating temperature can greatly enhance the sensors'
35 responses towards breath exposure.



36 **Keywords**

37 WO₃ nanowire sensors, metal nanoparticles, sensitivity enhancement, UV-light irradiation,
38 operating temperature, exhaled breath analysis.

39 **1. Introduction**

40 Exhaled breath is a valuable, non-invasive biological tool available for diagnosing and
41 monitoring medical conditions (Gardner et al., 2000; Adiguzel & Kulah 2015;
42 Lentka et al., 2016; Saidi et al., 2018). Its popularity in medicine can be demonstrated by an
43 increase in papers published in this area. Therefore, the development of advanced and cheap
44 sensors of high sensitivity towards low concentrations of VOCs in the exhaled breath is of
45 paramount importance. In this regard, MOS chemical gas sensors have emerged as a very
46 promising tool for monitoring low concentrations of gaseous compounds
47 (Konvalina & Haick 2014; Welearegay et al., 2016; Zhang et al., 2017), and they represent a
48 low-cost alternative as compared to other available analytical methods
49 (e.g., Gas Chromatography/Mass Spectrometry) that require expensive and bulky equipment.

50 Tungsten trioxide (WO₃), with a band gap of about 2.8 eV (Yun et al., 2016), is one of the most
51 important n-type MOSs, and it has been extensively used as a gas sensor material
52 for VOC detection (Righettoni et al., 2010; Choi et al., 2014; Kim et al., 2016;
53 Shendage et al., 2017). However, its selectivity and sensitivity are still too low for some
54 applications, such as breath analysis. The selectivity can be partially improved by using a set
55 of sensors with different cross-sensing performances and enhanced by reducing the particle size
56 to a range of 5 to 50 nm (Yamazoe, 1991; Shimizu and Egashira, 1999; Ederth et al., 2006).
57 Alternatively, the sensing potential of WO₃ sensors can be significantly improved by doping
58 the sensing layer with a small amount of metal nanoparticles (NPs), such as platinum, gold,
59 nickel, iron, etc. (Vallejos et al., 2013; Ahsan et al., 2013; Vilic and Llobet 2016). Metal doping



60 is considered a crucial option for diversifying the selectivity and improving the sensitivity of
61 the sensors. Nevertheless, the sensing performance of the WO_3 sensors must be further
62 optimised to satisfy the requirements for breath analysis applications.

63 WO_3 NW sensors generally operate at elevated temperatures because the detection mechanisms
64 are based on thermo-activated chemical reactions between the sensing film and the adsorbed
65 VOCs (Bendahan et al., 2007). Variation of the sensor's operating temperature may enhance its
66 sensitivity (Paulsson and Winqvist, 1999; Taurino et al., 2002; Ionescu and Llobet 2002;
67 Zhang et al., 2015). Besides, many researchers have proven that WO_3 sensor performance could
68 be influenced by a photocatalytic effect such as UV-light irradiation (Iliev et al., 2010;
69 Giberti et al., 2012; Smulko et al., 2015; Trawka et al., 2016; Gonzalez et al., 2016).
70 The sensitive film of the sensor absorbs the UV-light (Mishra et al., 2004), which provides a
71 further dissociation of the gaseous compounds and the consequent molecule adsorption
72 (Trawka et al., 2016). UV-light irradiation creates a charge transport that increases the density
73 of free electron-hole pairs (Karaduman et al., 2014; Xu et al., 2015). Therefore, it alters the
74 sensing layer. Moreover, the applied UV-light of selected wavelengths can modulate the
75 sensing properties in a different way due to various penetration depths, related to the applied
76 wavelength and morphology of the porous gas sensing layer. Altogether, the response of MOS
77 gas sensors can be successfully modified by UV-light that reduces the necessary heating energy
78 (Park et al., 2013; Espid and Taghipour, 2017).

79 In our paper, pristine and metal-doped WO_3 NWs were elaborated using aerosol-assisted
80 chemical vapour deposition (AACVD) and characterised by using Atomic Force Microscopy
81 (AFM), Scanning Electron Microscopy (SEM), Transmission Electron Microscopy (TEM) and
82 Energy Dispersive X-ray (EDX-ray). The effects of UV-light irradiation and operating
83 temperature selection were investigated regarding the analysis of exhaled breath.



84 2. Materials and methods

85 2.1. Sensor fabrication

86 AACVD was used to grow WO_3 NWs due to its simplicity and relatively low temperature
87 experimental conditions (Annanouch et al., 2013; Qadri et al., 2016). This method consists of
88 delivering a suitable precursor in the form of an aerosol into the reactor where the substrate is
89 mounted (Stoycheva et al. 2012).

90 In our study, six different sensors (*i.e.*, pristine WO_3 NWs and the following pool of metal-
91 doped WO_3 NWs: Pt/ WO_3 ; Au/Pt/ WO_3 ; Au/ WO_3 ; Ni/ WO_3 ; and Fe/ WO_3) were grown using
92 AACVD. Alumina substrates with Pt interdigitated electrodes on the front-side and
93 a Pt meander heater on the back-side were employed as sensing substrates from *CeramTec*®
94 (Marktredwitz, Germany). The substrates were successively cleaned with ethanol, acetone and
95 distilled water and dried with a nitrogen flow before they were placed inside the AACVD
96 reactor.

97 The layers of WO_3 NWs were prepared using tungsten hexacarbonyl (WC_6O_6) as a precursor
98 according to previous reported procedures (Annanouch et al., 2015; Thamri et al., 2016). The
99 experimental conditions for growing the six sensors are provided in Table 1. After nanomaterial
100 synthesis, the deposited films were annealed in an oven (Carbolite's calcination furnace
101 1200 °C | BWF) at 500 °C for 180 minutes under a constant flow of 200 mL/min of synthetic
102 air. This step was carried out in order to clean the surface of deposition residues and to stabilise
103 and crystallise the structure of the grown nanomaterials (Stankova et al., 2005; Ng et al., 2015).
104 Otherwise, the morphology and composition of the deposited films were characterised.
105 SEM measurements were performed using a FEI-ESEM Quanta 600 equipment (20 keV),
106 which was coupled to an EDX analyser from *Oxford Instruments*. A TEM analysis of the
107 Nanoparticles' sizes was done by JEOL JEM-1011 equipment with an accelerating energy of

108 100 keV while the structure of the deposited film was studied with AFM by means of a Keysight
109 5500 SPM.

110 AACVD reaction of WC_6O_6 with a mixture of acetone and methanol, inside a hot wall reactor,
111 resulted in the formation of blue-black WO_3 films. Applying the annealing process on these
112 films at 500 °C yielded yellow layers that indicated fully oxidised WO_3 . AFM analysis was used
113 in acoustic mode to assess a topography of the annealed surface of the deposited layers. Figure
114 1 presents orthogonal 3D images of the AFM topography of pristine and functionalised WO_3
115 films deposited onto alumina substrate which is scanned within an area of 10 μm^2 . It can be
116 seen that the maximal heights of the pristine WO_3 and Fe/ WO_3 NWs were 2.2 μm and 3.4 nm,
117 respectively (Fig. 1.a, Fig. 1.f). However, a significant reduction of surface roughness was
118 achieved by functionalising the sensing surface with metal nanoparticles (except for Fe
119 nanoparticles). Maximal heights of 762 nm, 713 nm, 991 nm and 505 nm for Pt/ WO_3 (Fig. 1.b),
120 Au/Pt/ WO_3 (Fig. 1.c), Au/ WO_3 (Fig. 1.d) and Ni/ WO_3 (Fig. 1.e) were obtained, respectively. In
121 all cases, AFM images showed complete coverage of the WO_3 films on the entire substrate
122 surface. It seems that the shape of the grains varied when changing the catalysts. Figure 2.a
123 shows a typical SEM image of the pristine WO_3 . It can be seen that the AACVD method
124 at 500 °C produced a layer of thick NWs (about 159 nm), with high density and quite
125 a homogeneous distribution on the entire substrate. In contrast, the films that contain Pt and/or
126 Au Nps exhibited a mixture of randomly distributed nanowires with a diameter ranging between
127 45 and 57 nm (Fig. 2.b, Fig. 2.c and Fig. 2.d). The layer of Ni/ WO_3 showed high density NWs
128 which were randomly distributed (Fig. 3.e). SEM data of Fe/ WO_3 also show NWs of various
129 sizes with a diameter ranging between 47 and 126 nm (Fig. 2.f). The AACVD yields a high
130 density of non-aligned nanowires, with a relatively homogeneous distribution containing small
131 pores over the studied surfaces. TEM of the deposited layers for pristine and functionalised
132 WO_3 displayed porous polycrystalline films in thinner structures, approximately as spherical or



133 cylindrical morphologies (Fig. 3). Nanowires and nanoparticles can be easily observed from
134 the recorded images. They appear well dispersed along the surface of the WO_3 films. The grain
135 diameters of the studied metal Nps were about 11 nm for Pt Nps (Fig. 3.b), 4.63 nm for the
136 alloy of Au/Pt Nps (Fig. 3.c), 3.97 nm for Au Nps (Fig. 3.d), 39 nm for Ni Nps (Fig. 3.e) and
137 8.22 nm for Fe Nps (Fig. 3.f). The results show that the set of the investigated sensors was
138 characterised by their high surface-to-volume ratio, which provides more surface area for both
139 chemical and physical interactions and therefore secures better sensitivity. The EDX spectrum
140 (Fig. 4) showed tungsten, oxygen and alumina (from the substrate) as the major peaks, and also
141 revealed the presence of metal nanoparticles on the surface of the sensing nanomaterials.
142 The percentages of metal nanostructures on the sensing films varied between 1% and 2% except
143 for Pt Nps where it is found within 6% to 7% due to presence of platinum connectors to
144 the substrate.

145 **2.2. Measurement set-up and conditions**

146 The main part of the presented experimental studies required a collection of exhaled breath
147 samples. To avoid any eventual artefacts, the breath samples were taken from the same
148 individual (non-smoker, adult man) using Tedlar® bags before any food or beverage
149 consumption. For this, the person took a deep breath, and breathed normally into the collection
150 bag before emptying his lungs. The breath sample was immediately transferred from the
151 collection bag into the gas chamber where the sensors were placed. This was done by pumping
152 the contents of each filled bag at a constant flow rate of 100 mL/min.

153 The experiments began by starting a flow of current through the sensors' heaters, corresponding
154 to the selected temperature, for 1000 s. Next, the sensors were exposed to the collected breath
155 sample for 40 min, and ended with the next 80 min of recovery under laboratory air using the
156 same flow rate of 100 mL/min. An exposure of the sensors' to the exhaled breath was done both
157 in dark and under UV-light irradiation. The sensors' conductance was continuously recorded at

158 a sampling rate of 1 Hz using an NI USB-6212 data acquisition board from *National*
159 *Instruments* (Texas, USA). The sensors' conductance was determined by measuring the DC
160 voltage across the sensor as part of a voltage divider with another resistor connected in series
161 and supplied by a DC voltage of 5 V. Figure 5 shows the circuit of the electrical current control
162 unit for the heaters of three sensors. This unit was repeated to supply DC current for the next
163 three heaters. The operating temperature was controlled by choosing the resistances of the
164 heaters (RH_n, n = 1 ... 6) with a selected current, adjusted by a potentiometer (P).
165 The experiment was performed using an array of six independent sensors in the dark and under
166 UV-light irradiation emitted by six OSV4YL5451B type diodes from *Opto-Supply*, China. Each
167 diode was mounted above the sensor at the same distance, and the optical power irradiating the
168 gas sensing layer was similar for each sensor.

169 The relative humidity and temperature inside the gas chamber was monitored during the
170 experiment with a HIH 4000-002 humidity sensor from *Honeywell*, USA, and a LM35DZ
171 temperature sensor from *Texas Instruments*, USA. The stability of the relative humidity
172 ($28\% \pm 5\%$) and temperature ($40^{\circ}\text{C} \pm 1^{\circ}\text{C}$) were recorded.

173 **3. Results and discussion**

174 Firstly, an experimental study was performed to find the most suitable operating temperatures
175 of the sensors that secured the best responses to exhaled breath samples. It was found that each
176 sensor has a range of operating temperatures, usually between 90°C and 120°C for pristine WO_3 ,
177 Pt/WO_3 and $\text{Au}/\text{Pt}/\text{WO}_3$ sensors (Subset #1), and between 140°C and 200°C for Au/WO_3 ,
178 Ni/WO_3 and Fe/WO_3 sensors (Subset #2). We selected temperature ranges to include the
179 optimal operating temperature for both sensor batches when exposed to breath samples.

180 Figure 6 shows the sensors' responses towards two successive breath exposures in the dark
181 (blue curves) and under UV-light irradiation (red curves); the sensors from Subset #1 operated

182 at 100 °C (Fig. 6.a, Fig. 6.b, Fig. 6.c), and the sensors from Subset #2 at 160 °C (Fig. 6.d,
183 Fig. 6.e and Fig. 6.f). Importantly, it can be seen that the sensors' responses became relatively
184 more intense under UV-light irradiation than in the dark. This effect can be measured by a
185 quotient Q of two conductances:

$$186 \quad Q = \frac{G_{F_{UV}}}{G_{F_{dark}}} \times 100\% \quad (1)$$

187 where:

- 188 • $G_{F_{UV}}$ – conductance observed after breath exposure under UV-light at the final
189 stage of the experiment,
- 190 • $G_{F_{dark}}$ – conductance observed after breath exposure in the dark at the final stage of
191 the experiment.

192 The quotient Q reached at least 150%. For the pristine WO_3 NW sensor, it reached $Q = 323\%$.
193 This result is associated with the photocatalytic reactions taking place in the sensing film and
194 with decomposition of the breath VOCs that are then adsorbed by the sensing material
195 (Trawka et al., 2016). When the photons' energy overtakes the energy band gap E_g of the
196 semiconductor, a generated electron (e^-) in the valence band is excited into the conduction band,
197 leaving a positive hole (h^+) in the valence band (Wu et al., 2015). The energy gap of WO_3 is
198 $E_g \approx 2.8$ eV, whereas the UV LEDs' wavelength is 394 nm, corresponding to a photon energy
199 of 3.15 eV. As a photon's energy emitted from the UV LEDs is higher than the energy gap for
200 WO_3 material, the sensor's conductance under UV-light irradiation should depend on the
201 interband transitions (Giberti et al., 2012).

202 When the sensors operated under UV-light irradiation, their responses were repeatable and their
203 recovery time was relatively short (Fig. 6). When the sensors operated under dark conditions,
204 their responses were much longer and exceeded the observation time. We can claim that the use

205 of UV-light irradiation accelerated the desorption rate of the VOCs adsorbed by the sensing
206 film before we switched to only the laboratory air. At the same time, UV-light quickened the
207 saturation of the investigated sensors when exposed to VOCs.

208 Figure 7 displays the responses to breath exposure of three investigated sensors operating at
209 selected temperatures. The presented data proves that under UV-light irradiation, the sensors
210 provide more repeatable responses and with more intense relative changes of conductance as
211 compared to their operation under dark conditions. This effect may be explained by intensified
212 desorption in the presence of UV light which accelerates cleansing of the sensors after breath
213 exposure. We have noticed that an increase of the sensor's operating temperature quickened its
214 response but decreased its relative changes of conductance. Thus, for the pristine WO_3 NW
215 sensor, the UV/dark ratio (*see* Eq. 1) increased from 342% at 90 °C to 419% at 110 °C (when
216 the sensor had not reached saturation during the experiment). At an operating temperature of
217 120 °C, the sensor response in the dark (blue curve) was more intense than at lower
218 temperatures, and therefore the UV/dark ratio of conductances decreased to 212% (Fig. 7.a,
219 Fig. 7.b and Fig. 7.c). In the case of the Au/Pt/ WO_3 sensor, an operating temperature of 90 °C
220 was too low to observe saturation or full recovery during the time of the experiment. The sensor
221 started to saturate at a temperature of 110 °C both in the dark and under UV-light operation.
222 UV-light irradiation assured a faster response, requiring only a few minutes, when compared to
223 dark conditions, requiring about 30 min (Fig. 7.d, Fig. 7.e). For this sensor, again, the operating
224 temperature of 120 °C assured more intense relative changes of conductance under dark
225 conditions than at lower temperatures (Fig. 7.f). This is also observed for the Au/ WO_3 sensor
226 at different operating temperatures. This sensor (Subset #2), showed that at an operating
227 temperature of 140 °C, saturation cannot be achieved in the dark nor under UV-light (Fig. 7.g).
228 Full saturation at an operating temperature of 180°C is reached after about 30 min of breath
229 exposure in the dark and after about 15 min under UV-light (Fig. 7.h). As a consequence,

230 the coefficient Q decreased from 333% at 180 °C to 181% at 200 °C (Fig. 7.i). These results
231 suggest that the presence of metal NPs on WO₃ NW surfaces could seriously improve the
232 sensor's sensitivity to exhaled breath exposure, while reducing its optimal operating
233 temperature.

234 Based on the time of response, operating temperature of the investigated sensors and relative
235 change of DC resistance, we may determine their sensitivity to the exhaled breath. Sensitivity
236 S can be defined as a relative change of conductance G_F measured at the end of observation
237 time (final conductance) in the ambient atmosphere of the exhaled breath and under dark
238 conditions or UV-light irradiation (by using the index "dark or UV") and referenced to
239 G measured in the ambient atmosphere of laboratory air:

$$240 \quad S = \frac{G_{F(\text{dark or UV})} - G_{0(\text{dark or UV})}}{G_{(\text{dark or UV})}} \times 100\% \quad (2)$$

241
242 All six sensors exhibited greater sensitivity when measured under UV-light irradiation at the
243 investigated operating temperatures. Subset #1 of the sensors (pristine WO₃, Pt/WO₃ and
244 Au/Pt/WO₃) reached higher sensitivities towards breath exposures at 100 °C both in the dark
245 and under UV-light irradiation (Fig. 8.a, Fig. 8.b), which drastically decreased at 110 °C and
246 further at 120 °C under UV-light irradiation. In the case of the sensors from Subset #2 (Au/WO₃,
247 Ni/WO₃ and Fe/WO₃), their sensitivity changed slightly at the considered operating
248 temperatures and in the dark (Fig. 8.c), while under UV-light irradiation, the changes were
249 much more intense and the greatest sensitivity was observed at 160 °C (Fig. 8.d). The most
250 significant difference between the sensitivity in the dark and under UV-light irradiation was
251 found for the Au/WO₃ sensor, which increased from 88.9 % to 216.9% at 160 °C.

252 The reported results mean that a proper combination of the sensors' heating and UV-irradiation
253 may play a crucial role in enhancing MOS WO₃ sensors' sensitivity towards the detection of



254 the VOC's in the exhaled breath. Their functionalisation by metal-doped nanoparticles is also
255 important to determine the sensors' optimal operating temperature, together with the sensors'
256 sensitivity and selectivity.

257 **4. Conclusions**

258 Our experimental study presents the first ever report of UV-irradiation combined with a
259 selection of the sensors' operating temperatures to enhance exhaled breath detection by WO₃
260 NW sensors decorated by selected metal dopants. The study was performed on both pristine
261 and NP-doped WO₃ NWs grown by AACVD on alumina substrates and characterised by AFM,
262 SEM, TEM and EDX-ray. All sensors clearly responded to the exhaled breath, both in the dark
263 and under UV-light irradiation. In addition, their responses were repeatable and determined by
264 their operating temperatures. The experimental results revealed that the most sensitive sensor
265 towards the exhaled breath samples was the Au-doped WO₃ NWs operating at 160 °C.
266 It reached a sensitivity as high as $S = 216.9\%$ under UV-light irradiation. These promising
267 results may be a way for further development of low-cost, low-power consumption and highly
268 sensitive gas sensors for medical applications.

269 **Acknowledgments**

270 We would like to thank Moulay Ismaïl University for financial support of the project "Research
271 support". This work has been funded in part by TROPSENSE under the H2020-MSCA-RISE-
272 2014 project, grant agreement number: 645758.

273 **References**

274 Adiguzel, Y., & Kulah, H. (2015). Breath sensors for lung cancer diagnosis. *Biosensors and*
275 *Bioelectronics*, 65, 121-138.



276 Ahsan, M., Ahmad, M. Z., Tesfamichael, T., Bell, J., & Yarlagadda, P. K. (2013). Ethanol
277 sensitivity of thermally evaporated nanostructured WO₃ thin films doped and implanted with
278 Fe. In *Applied Mechanics and Materials* (Vol. 333, pp. 1938-1945). Trans Tech Publications.

279 Annanouch, F. E., Gràcia, I., Figueras, E., Llobet, E., Cané, C., & Vallejos, S. (2015). Localized
280 aerosol-assisted CVD of nanomaterials for the fabrication of monolithic gas sensor microarrays.
281 *Sensors and Actuators B: Chemical*, 216, 374-383.

282 Annanouch, F. E., Vallejos, S., Stoycheva, T., Blackman, C., & Llobet, E. (2013). Aerosol
283 assisted chemical vapour deposition of gas-sensitive nanomaterials. *Thin Solid Films*, 548,
284 703-709.

285 Bendahan, M., Guerin, J., Boulmani, R., & Aguir, K. (2007). WO₃ sensor response according
286 to operating temperature: experiment and modeling. *Sensors and Actuators B: Chemical*,
287 124(1), 24-29.

288 Choi, S. J., Fuchs, F., Demadrille, R., Grévin, B., Jang, B. H., Lee, S. J., & Kim, I. D. (2014).
289 Fast responding exhaled-breath sensors using WO₃ hemitubes functionalized by graphene-
290 based electronic sensitizers for diagnosis of diseases. *ACS Applied Materials & Interfaces*,
291 6(12), 9061-9070.

292 Espid, E., & Taghipour, F. (2017). Development of highly sensitive ZnO/In₂O₃ composite gas
293 sensor activated by UV-LED. *Sensors and Actuators B: Chemical*, 241, 828-839.

294 Gardner, J. W., Shin, H. W., & Hines, E. L. (2000). An electronic nose system to diagnose
295 illness. *Sensors and Actuators B: Chemical*, 70(1), 19-24.

296 Giberti, A., Malagù, C., & Guidi, V. (2012). WO₃ sensing properties enhanced by UV
297 illumination: an evidence of surface effect. *Sensors and Actuators B: Chemical*, 165(1), 59-61.



- 298 Gonzalez, O., Welearegay, T., Llobet, E., & Vilanova, X. (2016). Pulsed UV Light Activated
299 Gas Sensing in Tungsten Oxide Nanowires. *Procedia Engineering*, 168, 351-354.
- 300 Iliev, V., Tomova, D., Rakovsky, S., Eliyas, A., & Puma, G. L. (2010). Enhancement of
301 photocatalytic oxidation of oxalic acid by gold modified WO_3/TiO_2 photocatalysts under UV
302 and visible light irradiation. *Journal of Molecular Catalysis A: Chemical*, 327(1), 51-57.
- 303 Ionescu, R., & Llobet, E. (2002). Wavelet transform-based fast feature extraction from
304 temperature modulated semiconductor gas sensors. *Sensors and Actuators B: Chemical*, 81(2),
305 289-295.
- 306 Karaduman, I., Yıldız, D. E., Sincar, M. M., & Acar, S. (2014). UV light activated gas sensor
307 for NO_2 detection. *Materials Science in Semiconductor Processing*, 28, 43-47.
- 308 Konvalina, G., & Haick, H. (2014). Sensors for breath testing: from nanomaterials to
309 comprehensive disease detection. *Acc. Chem. Res*, 47(1), 66-76.
- 310 Kim, S. J., Choi, S. J., Jang, J. S., Kim, N. H., Hakim, M., Tuller, H. L., & Kim, I. D. (2016).
311 Mesoporous WO_3 nanofibers with protein-templated nanoscale catalysts for detection of trace
312 biomarkers in exhaled breath. *ACS nano*, 10(6), 5891-5899.
- 313 Lentka, Ł., Kotarski, M., Smulko, J., Cindemir, U., Topalian, Z., Granqvist, C. G., Raul
314 Calavia., & Ionescu, R. (2016). Fluctuation-enhanced sensing with organically functionalized
315 gold nanoparticle gas sensors targeting biomedical applications. *Talanta*, 160, 9-14.
- 316 Mishra, S., Ghanshyam, C., Ram, N., Bajpai, R. P., & Bedi, R. K. (2004). Detection mechanism
317 of metal oxide gas sensor under UV radiation. *Sensors and Actuators B: Chemical*, 97(2),
318 387-390.



319 Ng, C. Y., Razak, K. A., & Lockman, Z. (2015). Effect of annealing temperature on anodized
320 nanoporous WO₃. *Journal of Porous Materials*, 22(2), 537-544.

321 Park, S., An, S., Ko, H., Lee, S., & Lee, C. (2013). Synthesis, structure, and UV-enhanced gas
322 sensing properties of Au-functionalized ZnS nanowires. *Sensors and Actuators B: Chemical*,
323 188, 1270-1276.

324 Paulsson, N., Larsson, E., & Winquist, F. (2000). Extraction and selection of parameters for
325 evaluation of breath alcohol measurement with an electronic nose. *Sensors and Actuators A:*
326 *Physical*, 84(3), 187-197.

327 Paulsson, N., & Winquist, F. (1999). Analysis of breath alcohol with a multisensor array:
328 instrumental setup, characterization and evaluation. *Forensic science international*, 105(2),
329 95-114.

330 Qadri, M. U., Annanouch, F. E., Aguiló, M., Díaz, F., Borull, J. F., Pujol, M. C., & Llobet, E.
331 (2016). Metal Decorated WO₃ Nanoneedles Fabricated by Aerosol Assisted Chemical Vapor
332 Deposition for Optical Gas Sensing. *Journal of Nanoscience and Nanotechnology*, 16(9),
333 10125-10132.

334 Righettoni, M., Tricoli, A., & Pratsinis, S. E. (2010). Si: WO₃ sensors for highly selective
335 detection of acetone for easy diagnosis of diabetes by breath analysis. *Analytical chemistry*,
336 82(9), 3581-3587.

337 Saidi, T., Zaim, O., Moufid, M., El Bari, N., Ionescu, R., & Bouchikhi, B. (2018). Exhaled
338 breath analysis using electronic nose and gas chromatography-mass spectrometry for non-
339 invasive diagnosis of chronic kidney disease, diabetes mellitus and healthy subjects. *Sensors*
340 *and Actuators B: Chemical*, 257, 178-188.



341 Shendage, S. S., Patil, V. L., Vanalakar, S. A., Patil, S. P., Harale, N. S., Bhosale, J. L., ... &
342 Patil, P. S. (2017). Sensitive and selective NO₂ gas sensor based on WO₃ nanoplates. *Sensors*
343 and *Actuators B: Chemical*, 240, 426-433.

344 Shimizu, Y., & Egashira, M. (1999). Basic aspects and challenges of semiconductor gas
345 sensors. *Mrs Bulletin*, 24(6), 18-24.

346 Ederth, J., Smulko, J. M., Kish, L. B., Heszler, P., & Granqvist, C. G. (2006). Comparison of
347 classical and fluctuation-enhanced gas sensing with Pd_xWO₃ nanoparticle films. *Sensors and*
348 *Actuators B: Chemical*, 113(1), 310-315.

349 Smulko, J. M., Trawka, M., Granqvist, C. G., Ionescu, R., Annanouch, F., Llobet, E., & Kish,
350 L. B. (2015). New approaches for improving selectivity and sensitivity of resistive gas sensors:
351 a review. *Sensor Review*, 35(4), 340-347.

352 Stankova, M., Vilanova, X., Llobet, E., Calderer, J., Bittencourt, C., Pireaux, J. J., & Correig,
353 X. (2005). Influence of the annealing and operating temperatures on the gas-sensing properties
354 of RF sputtered WO₃ thin-film sensors. *Sensors and Actuators B: Chemical*, 105(2), 271-277.

355 Stoycheva, T., Vallejosa, S., Blackman, C., Moniz, S. J. A., Calderer, J., et al. (2012)
356 Important considerations for effective gas sensors based on metal oxide nanoneedles films.
357 *Sensors and Actuators B* 161: 406-413.

358 Stoycheva, T., Annanouch, F. E., Gràcia, I., Llobet, E., Blackman, C., Correig, X., & Vallejos,
359 S. (2014). Micromachined gas sensors based on tungsten oxide nanoneedles directly integrated
360 via aerosol assisted CVD. *Sensors and Actuators B: Chemical*, 198, 210-218.

361 Taurino, A., Capone, S., Distante, C., Epifani, M., Rella, R., & Siciliano, P. (2002). Recognition
362 of olive oils by means of an integrated sol-gel SnO₂ electronic nose. *Thin Solid Films*, 418(1),
363 59-65.



- 364 Thamri, A., Baccar, H., Annanouch, F. E., Llobet, E., & Abdelghani, A. (2016). Methanol,
365 Ethanol and Acetone Sensing Using AACVD-grown Tungsten Oxide Nanoneedles. *J Nanomed*
366 *Nanotechnol*, 7(380), 2.
- 367 Trawka, M., Smulko, J., Hasse, L., Granqvist, C. G., Annanouch, F. E., & Ionescu, R. (2016).
368 Fluctuation enhanced gas sensing with WO₃-based nanoparticle gas sensors modulated by UV
369 light at selected wavelengths. *Sensors and Actuators B: Chemical*, 234, 453-461.
- 370 Vallejos, S., Umek, P., Stoycheva, T., Annanouch, F., Llobet, E., Correig, X., ... & Blackman,
371 C. (2013). Single-Step Deposition of Au-and Pt-Nanoparticle-Functionalized Tungsten Oxide
372 Nanoneedles Synthesized Via Aerosol-Assisted CVD, and Used for Fabrication of Selective
373 Gas Microsensor Arrays. *Advanced Functional Materials*, 23(10), 1313-1322.
- 374 Vilic, T., & Llobet, E. (2016). Nickel Doped WO₃ Nanoneedles Deposited by a Single Step
375 AACVD for Gas Sensing Applications. *Procedia Engineering*, 168, 206-210.
- 376 Welearegay, T. G., Gualdrón, O. E., Jaimes, A. L., Cáceres, J. M., Pugliese, G., Cindemir, U.,
377 ... & Ionescu, R. (2016). Ultrapure Organically Modified Gold Nanoparticles for Breath
378 Analysis. *Procedia Engineering*, 168, 133-136.
- 379 Wu, W., Jiang, C., & Roy, V. A. (2015). Recent progress in magnetic iron oxide–semiconductor
380 composite nanomaterials as promising photocatalysts. *Nanoscale*, 7(1), 38-58.
- 381 Xu, S., Sun, F., Yang, S., Pan, Z., Long, J., & Gu, F. (2015). Fabrication of SnO₂-Reduced
382 Graphite Oxide Monolayer-Ordered Porous Film Gas Sensor with Tunable Sensitivity through
383 Ultra-Violet Light Irradiation. *Scientific reports*, 5, 1-8.
- 384 Yamazoe, N. (1991). New approaches for improving semiconductor gas sensors. *Sensors and*
385 *Actuators B: Chemical*, 5(1-4), 7-19.



- 386 Yu-De, W., Zhan-Xian, C., Yan-Feng, L., Zhen-Lai, Z., & Xing-Hui, W. (2001). Electrical and
387 gas-sensing properties of WO₃ semiconductor material. *Solid-State Electronics*, 45(5), 639-644.
- 388 Yun, G., Balamurugan, M., Kim, H. S., Ahn, K. S., & Kang, S. H. (2016). Role of WO₃ layers
389 electrodeposited on SnO₂ inverse opal skeletons in photoelectrochemical water splitting.
390 *The Journal of Physical Chemistry C*, 120(11), 5906-5915.
- 391 Zhang, G., & Xie, C. (2015). A novel method in the gas identification by using WO₃ gas sensor
392 based on the temperature-programmed technique. *Sensors and Actuators B: Chemical*, 206,
393 220-229.
- 394 Zhang, J., Qin, Z., Zeng, D., & Xie, C. (2017). Metal-oxide-semiconductor based gas sensors:
395 screening, preparation, and integration. *Physical Chemistry Chemical Physics*, 19(9),
396 6313-6329.
- 397 Smulko, J. M., & Kish, L. B. (2004). Higher-order statistics for fluctuation-enhanced gas-
398 sensing. *Sensors and Materials*, 16(6), 291-299.



Highlights

- AACVD was carried out to produce pristine and differently functionalised WO₃
- The grown sensors were characterised with AFM, SEM, TEM and EDX-ray
- UV-light irradiation enhanced the sensors' responses towards breath exposure
- The most sensitive sensor for breath was the Au-doped WO₃ and operating at 160 °C

Figure 1 AFM topographies of the sensors' surfaces of: (a) pristine WO_3 ; (b) Pt/WO_3 ; (c) $\text{Au}/\text{Pt}/\text{WO}_3$; (d) Au/WO_3 ; (e) Ni/WO_3 ; (f) Fe/WO_3 .

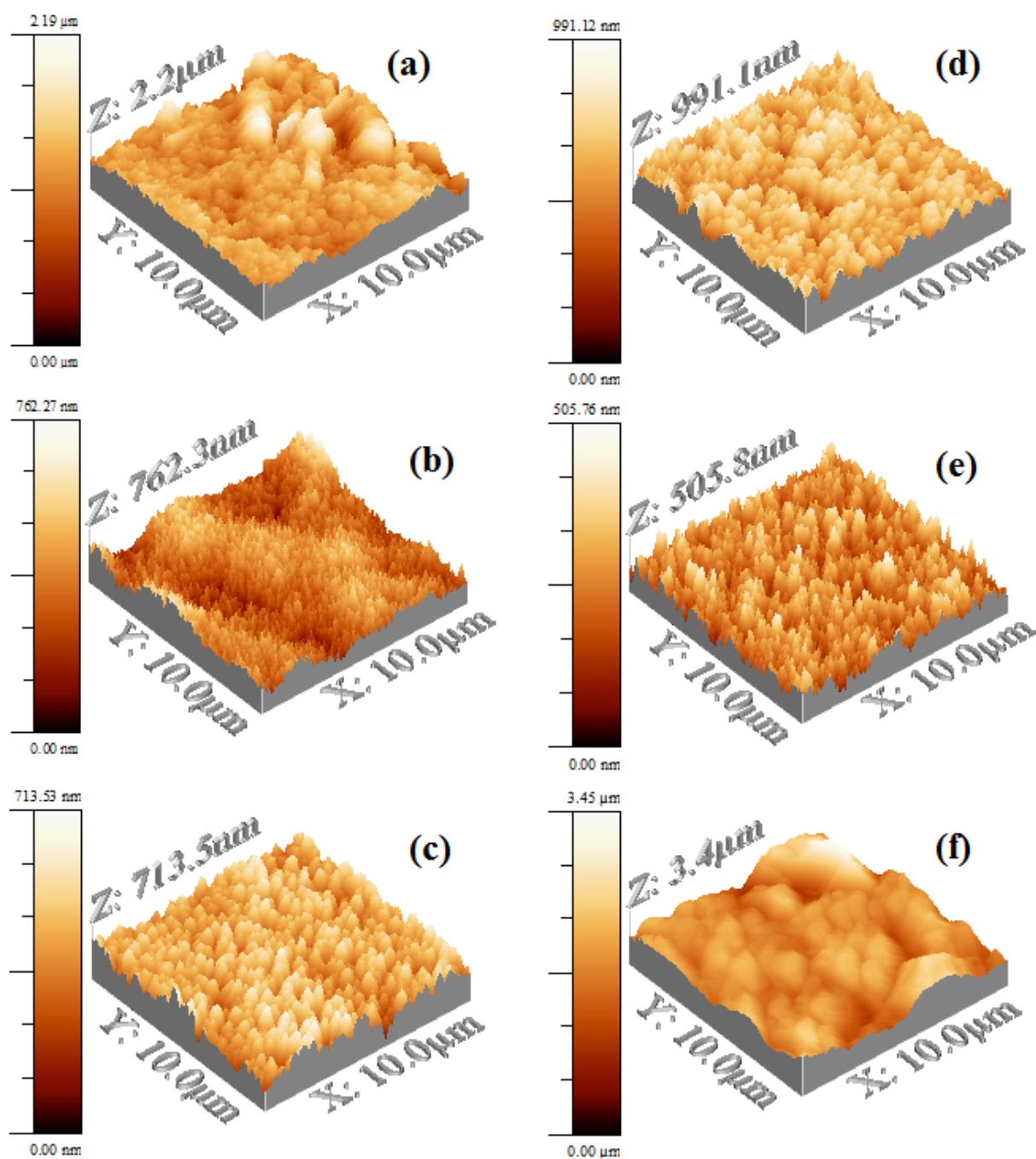


Figure 2 Typical SEM images of sensing areas of: (a) pristine WO_3 ; (b) Pt/WO_3 ; (c) $\text{Au}/\text{Pt}/\text{WO}_3$; (d) Au/WO_3 ; (e) Ni/WO_3 ; (f) Fe/WO_3 .

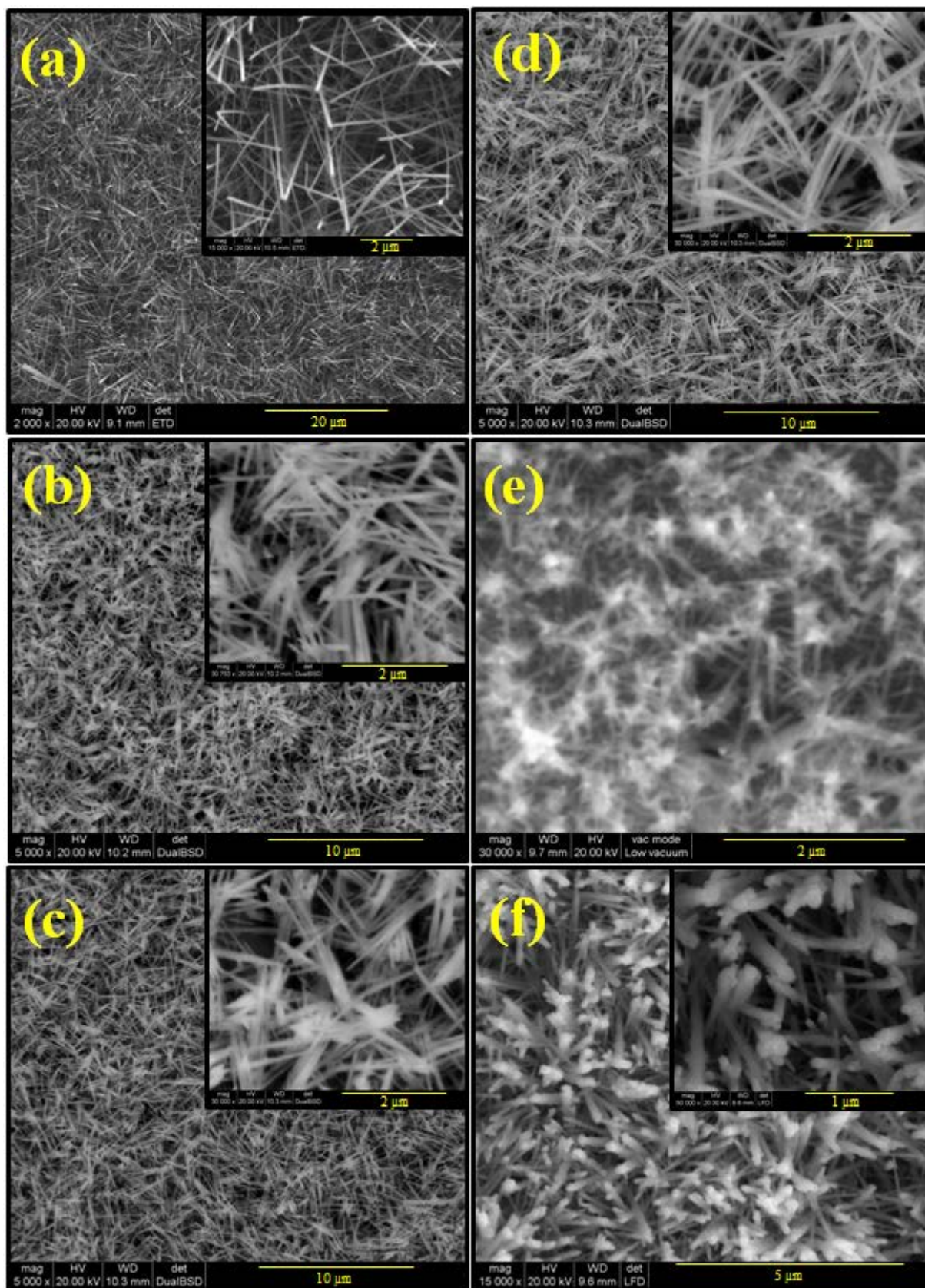


Figure 3 TEM images of the sensitive films of: (a) pristine WO_3 ; (b) Pt/WO_3 ; (c) $\text{Au}/\text{Pt}/\text{WO}_3$; (d) Au/WO_3 ; (e) Ni/WO_3 ; (f) Fe/WO_3 .

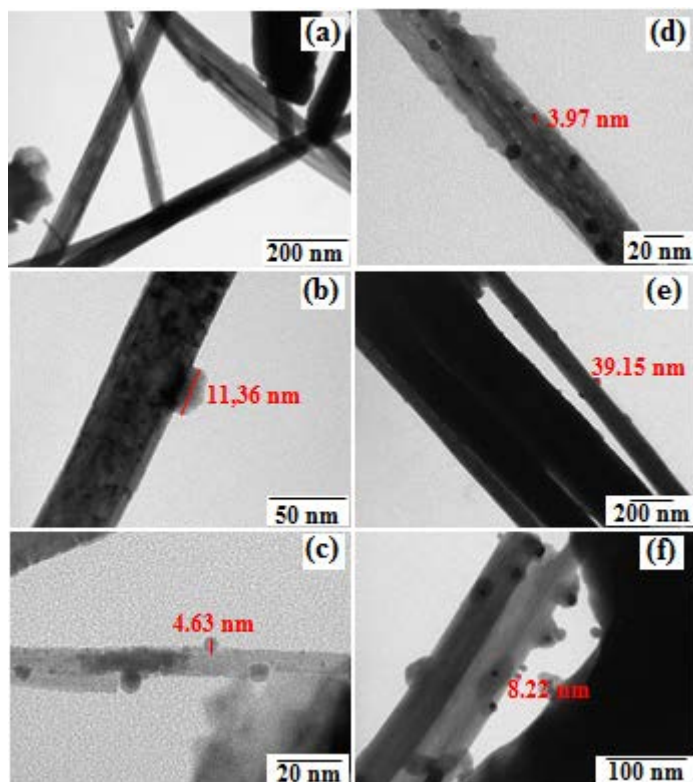


Figure 4 EDX-ray spectrum of the six sensors: (a) pristine WO_3 ; (b) Pt/WO_3 ; (c) $\text{Au}/\text{Pt}/\text{WO}_3$; (d) Au/WO_3 ; (e) Ni/WO_3 ; (f) Fe/WO_3 .

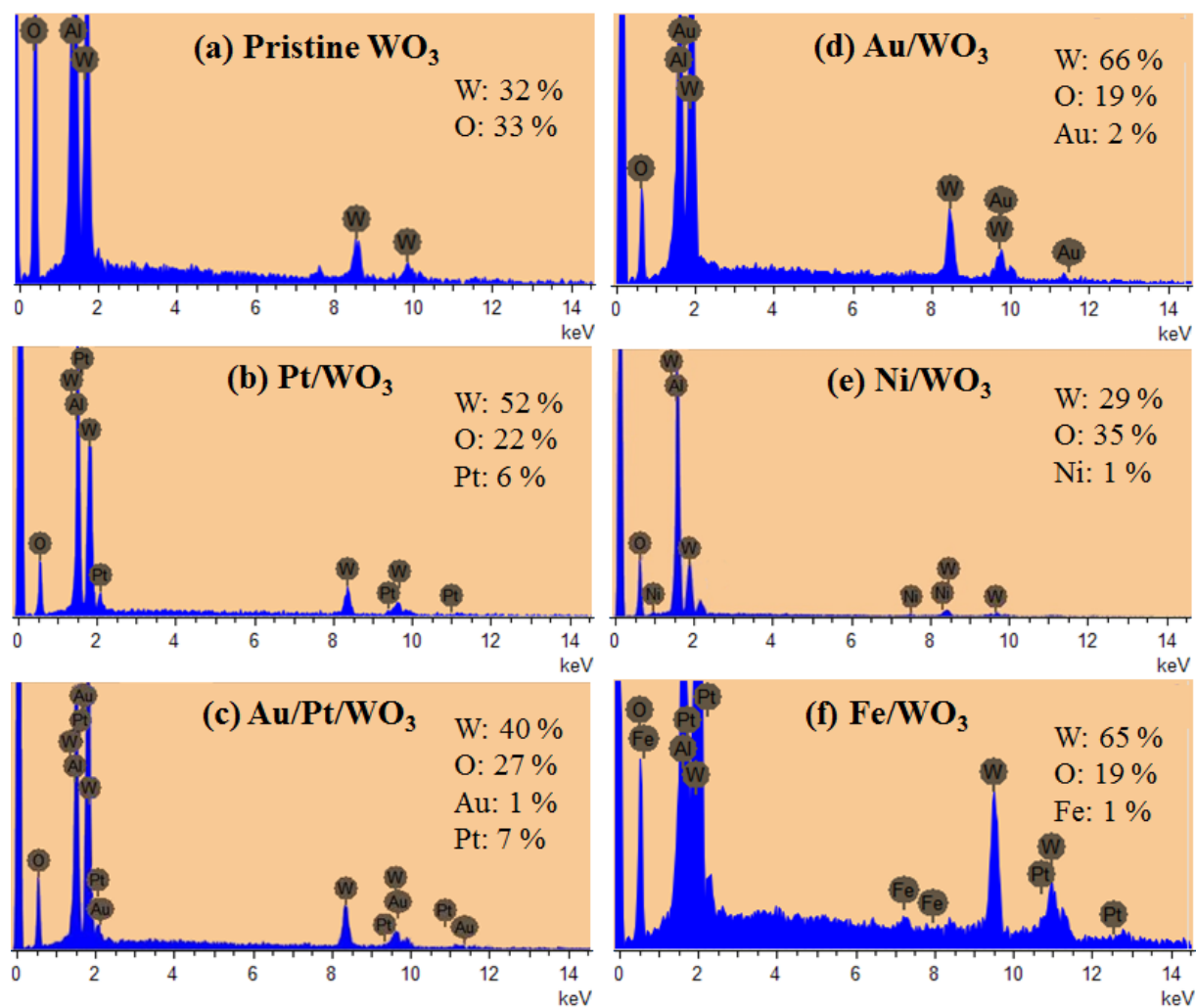


Figure 5 Electronic conditioning circuit for monitoring the current of three sensors' heaters connected in series.

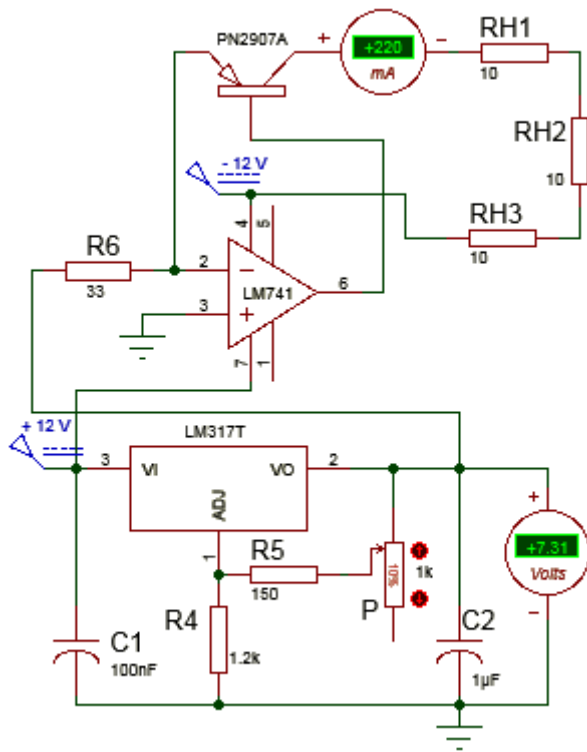


Figure 6 Sensors responses towards two repeated breath exposures in the dark (blue curves) and under UV-light illumination (red curves) for: (a) Pristine WO_3 ; (b) Pt/WO_3 ; (c) $\text{Au}/\text{Pt}/\text{WO}_3$; (d) Au/WO_3 ; (e) Ni/WO_3 ; (f) Fe/WO_3 . Sensors (a) to (c) were operated at 100°C , and sensors (d) to (f) at 160°C .

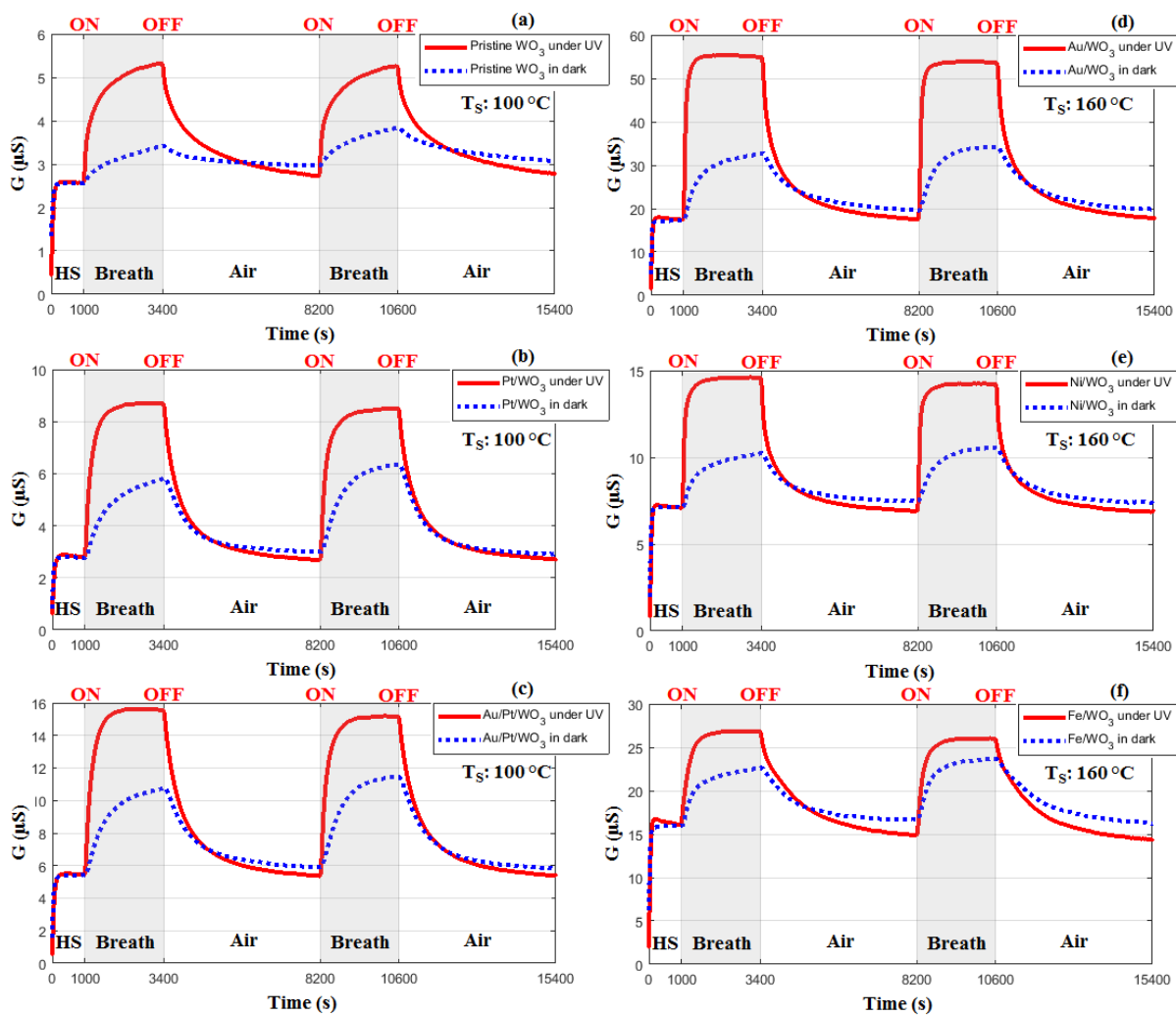


Figure 7 Sensors responses towards two repeated breath exposures in the dark (blue curves) and under UV-light illumination (red curves) for Pristine WO_3 sensor operated at: (a) 90°C ; (b) 110°C ; (c) 120°C ; Au/Pt/WO_3 sensor operated at: (d) 90°C , (e) 110°C ; (f) 120°C ; Au/WO_3 sensor operated at: (g) 140°C ; (h) 180°C ; (i) 200°C .

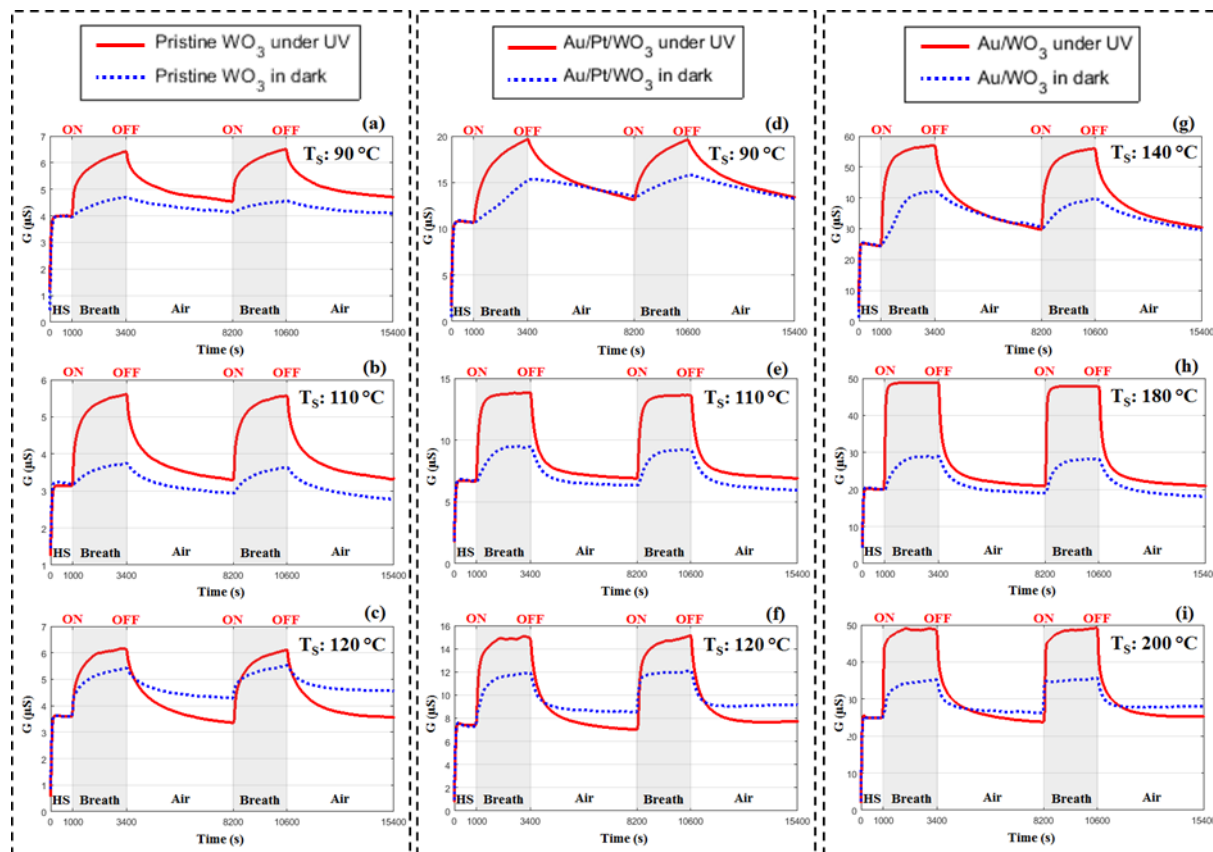


Figure 8 Sensors sensitivities in the presence of breath exposure at four different temperatures for pristine WO_3 , Pt/WO_3 , $\text{Au}/\text{Pt}/\text{WO}_3$: (a) in dark, (b) under UV irradiation; and Au/WO_3 , Ni/WO_3 , Fe/WO_3 : (c) in dark, (d) under UV irradiation.

